Processing and Application of Ceramics 13 [2] (2019) 189–201
https://doi.org/10.2298/PAC1902189B



# Stable $CuCrO_2$ nanoparticles – ZnO fibres p-n heterostructure system for effective photocatalytic activity

Elif Baylan, Hasan Akyildiz, Ozlem Altintas Yildirim*

*Konya Technical University, Faculty of Engineering and Natural Sciences, Department of Metallurgical and Materials Engineering, Konya, Turkey*

Received 18 December 2018; Received in revised form 25 March 2019; Accepted 31 May 2019

## Abstract

*Heterostructured photocatalysts were fabricated by coupling electrospun n-type ZnO fibres and hydrothermally derived p-type $CuCrO_2$ nanoparticles. The effect of the amount of $CuCrO_2$ nanoparticles on the photocatalytic activity of the heterostructured photocatalyst was systematically investigated. The formation of the heterojunctions between the two semiconductors was revealed via detailed XRD, XPS, TEM and optical property measurements. The experimental results indicated that the optimal $CuCrO_2$ amount in the composite photocatalyst was 1.0 wt.% due to the optimum doping and surface coverage, higher absorption onset edge, larger absorption intensity and optimum band gap energy. This composite photocatalyst, fabricated by drop casting of $CuCrO_2$ nanoparticle dispersion on ZnO fibres, displayed 30% higher rate constant (k) value compared to the pure ZnO fibres in the degradation of methylene blue dye molecules and reached 93.4% decomposition in 1 h under UV-visible light exposure. The obtained results are highly encouraging in comparison to only UV/light active p-n heterostructured photocatalysts previously reported in literature. Therefore, we believe that the proposed approach here opened the way for simple synthesis of highly-efficient visible light active heterostructured semiconductor photocatalyst systems.*

***Keywords:*** *photocatalytic activity, p-n heterojunctions, ZnO fibre, $CuCrO_2$ delafossite, photocatalyst*

## I. Introduction

Semiconductor-mediated photocatalysis has been attracted great scientific and technological attention in the context of wastewater remediation since the process involves conversion of solar energy directly into chemical energy [1]. This energy can be used and capable of removing a wide range of organic pollutants in water via redox reactions [2]. An efficient semiconductor photocatalyst should be excited by exposing it to a light source to create sufficient amount of electron-hole ($e^-$–$h^+$) pairs, possess various mechanisms to prevent recombination of these charges and migration of them toward the surface where the redox reactions occur [3].

Among the various semiconductor photocatalysts proposed, ZnO is one of the most popular oxides due to its low cost, high photochemical stability and photocatalytic performance [4]. ZnO is an n-type semiconductor with a wide direct band gap (3.37 eV) and can be produced in a variety of forms, e.g. thin film, particles and fibre aiming photocatalysis applications [5–7]. However, due to its wide bandgap, the main absorption occurs in ultraviolet (UV) wavelengths, which accounts for only 3–5% of total radiation from the Sun. While a semiconductor material can only be excited and generate $e^-$–$h^+$ pairs under super band irradiation, modifying the absorption range of ZnO towards the visible region is an efficient way to improve its photocatalytic efficiency [8].

Further on, any modification that would inhibit the recombination or promote the separation and migration of photogenerated $e^-$–$h^+$ pairs will improve the photocatalytic efficiency of ZnO [9,10]. This may be achieved simply by two approaches, i.e. by doping to modify its wide bandgap or by producing heterostructures with ZnO [11]. In the first approach, doping may be attained via incorporation of metal ions into the crystal structure of ZnO. Incorporation of a metal ion into the lattice generally creates extra energy levels and these levels act as $e^-$–$h^+$ scavengers and led to increase in the

* Corresponding authors: tel: +90 332 223-2207,
e-mail: *ozlemaltintas@gmail.com, oayildirim@ktun.edu.tr*

lifetime of charge carriers [12]. Since transition metals and rare-earth elements possess fully occupied *d*- or *f*-orbitals, they are used as dopants in ZnO for photocatalytic applications [5,13]. The second approach may include fabrication of ZnO-metal or ZnO-semiconductor heterostructures. In the case of ZnO-metal heterostructures, generally nanocrystals of noble metals (Au, Ag or Pt) are coated on the surface of pristine ZnO. As a result, a Schottky junction forms between the ZnO and the metal nanoparticles and then the metal act as a carrier trap centre. This promotes interfacial charge transfer and thus enhances the electron-hole pair separation [14–17]. On the other hand, ZnO-semiconductor heterostructures can be achieved by coupling ZnO with other semiconductors, such as $TiO_2$, $SnO_2$, $CeO_2$, ZnS and CdS. The interface between ZnO and the others may be classified into three groups according to the relative positions of the conduction and valence band of ZnO and the coupling semiconductor [9]. In this context, ZnO can be coupled with a p-type semiconductor having a proper band gap to form a p-n junction. The difference in their band levels may then create an inner electric field and this built-in potential can be used to promote separation and transportation of the photogenerated charge carriers [18–21].

In addition to above discussion on ZnO, delafossite structured oxides, which are denoted by the general formula as $AMO_2$ (A = $Cu^+$ or $Ag^+$, $d^{10}$ metal ions, and M = $Al^{3+}$, $Ga^{3+}$, $In^{3+}$, $Fe^{3+}$, $Co^{3+}$, $B^{3+}$, $Cr^{3+}$, and etc.) are mostly recognized by their unusual p-type electrical conductivity and transparency in the visible region. Therefore, they are considered as an important and potential material class for a variety of optoelectronic applications [22,23]. According to the reported data in the literature, the direct and indirect band gaps of $CuCrO_2$ vary with the processing parameters and measurements in the range of 2.95–3.35 eV and 1.28–2.63 eV, respectively [24]. Although the true value of the band gap of $CuCrO_2$ has been controversy, it can theoretically absorb light in the visible region and it has been shown to be active under solar light in some applications such as water splitting and depollution via photocatalysis reactions [25–27]. Recently, Ahmad *et al.* [27] prepared pure $CuCrO_2$ nanoparticles via polymeric citrate precursor method and showed that ~88% methylene blue (MB) dye can be degraded after just 1.5 h on these nanoparticles under natural sun light exposure. Nevertheless, there are only a few studies published in the literature on the heterostructures of $CuCrO_2$ with other semiconductors including $CuCrO_2$-ZnO for the reduction of Cr(IV) to Cr(III) [28] and water splitting [29], $CuCrO_2$-$WO_3$ for visible light HCl splitting [30], and $CuCrO_2$-$TiO_2$ for photodegradation of MB under ultraviolet (UV) irradiation [31]. In addition, in a very recent study, Cossuet *et al.* [32] reported on the fabrication of ZnO/$CuCrO_2$ core-shell nanowire heterostructures. They showed that ZnO/$CuCrO_2$ heterostructures can be used effectively as a fast response and self-powered UV-photodetector. These examples imply that heterostructures of $CuCrO_2$ with other semiconductors have potential use in a wide range of applications.

The photocatalytic activity of oxide semiconductors depends on their size and morphology. With a decrease in the particle size of the material, the specific surface area increases which provides interaction of higher number of active sites with the pollutant molecules [34]. Among other nanomaterial forms, nanofibres are advantageous due to their distinguished properties such as higher stiffness and tensile stress, high surface area and quick migration routes for charge carriers due to their 1D morphology [18]. Mechanical durability provides flexibility during the activity measurements in terms of the photocatalyst design and also recycling possibility without a significant decrease in their photocatalytic activity. Further, the size and morphology of the nanofibres may promote the separation of electron-hole pairs. These unique features also provide flexibility in the surface modification of these materials [35,36]. Thus, ZnO fibres can easily be doped via metal and non-metal dopants, coupled with metal nanoparticles and other semiconductors to improve the photocatalytic efficiency. Up to now, 1D ZnO nanostructures have been prepared using chemical vapour deposition, template assisted sol-gel, hydrothermal synthesis, and electrospinning based methods [37–40]. Among them, electrospinning is a simple and versatile processing route which has been used for the production of n-type ZnO and other ceramic nanofibres in a variety of composition and sizes [41–44].

In this study, a series of $CuCrO_2$ wrapped ZnO fibres were successfully prepared and employed as an efficient photocatalyst in the degradation of MB dye under UV-visible light irradiation, for the first time. In order to fabricate the heterostructured photocatalyst, in the first step $CuCrO_2$ nanoparticles were prepared via conventional hydrothermal synthesis. Then these nanoparticles were dispersed in alcohol to achieve ZnO fibres wrapped with up to 1.2 wt.% $CuCrO_2$. The formation of p-n heterostructures was revealed via detailed XRD, XPS, TEM and UV-vis spectrophotometer measurements.

## II. Experimental procedure

### *2.1. Synthesis of ZnO fibres*

The production steps for ZnO fibres is given in Fig. 1. The synthesis was performed in two steps by using zinc acetate dihydrate ($Zn(CH_3COO)_2 \cdot 2\,H_2O$, 98%, Sigma Aldrich), polyvinyl alcohol (PVA, $M_w$ = 88000, Alfa Aesar) and ultrapure deionized water. All reagents were used without further purification. Initially, an aqueous PVA solution (15 wt.%) was prepared at 70 °C under mild stirring conditions for 4 h. Meanwhile, 1.0 g of $Zn(CH_3COO)_2 \cdot 2\,H_2O$ was dissolved in 4.5 ml of deionized water and then this was added to the above mentioned PVA solution at room temperature. This final mixture was then continuously stirred for about 20 h

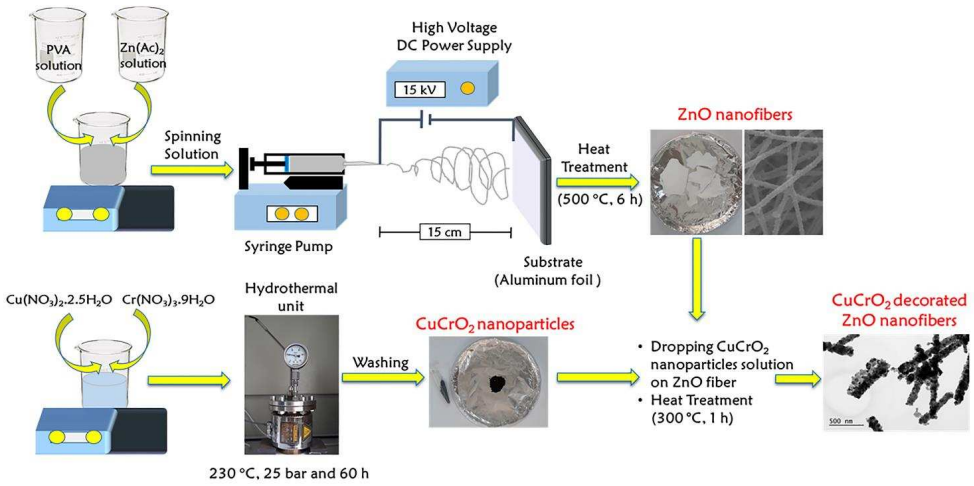


**Figure 1. Schematic illustration of the synthesis procedure for $CuCrO_2$ nanoparticles-ZnO fibres p-n heterojunction samples**

to achieve a homogenous and clear spinning solution. Electrospinning was performed using a hygienic syringe with a 0.7 mm diameter tip. The solution was pumped with a flow rate of 0.4 ml/h on an aluminium foil substrate placed at a distance of 15 cm. The composite fibres were collected under an applied potential of 15 kV. For each experiment, 2 ml of solution was electrospun on $10 \times 10\,cm^2$ of the foil substrate. In the second step, these samples were then loaded into a box furnace and heated to 500 °C with a heating rate of 1 °C/min. After 6 h of annealing, the samples were furnace cooled to room temperature. Organic removal step led to the formation of self-standing pure white and relatively large pieces of fibres. These pieces were weighed and cut into pieces (e.g. $2 \times 2\,cm^2$) and stored under environmental conditions for further use.

### 2.2. *Synthesis of $CuCrO_2$ nanoparticles*

$CuCrO_2$ nanoparticles were obtained according to the synthesis procedure given in Fig. 1. The production of delafossite nanoparticles was carried out in a custom made hydrothermal unit described in detail elsewhere [45,46]. Copper nitrate hemipentahydrate ($Cu(NO_3)_2 \cdot 2.5\,H_2O$, 98%, Alfa Aesar), chromium nitrate nonahydrate ($Cr(NO_3)_3 \cdot 9\,H_2O$, 99%, Sigma Aldrich) and sodium hydroxide (NaOH pellets, 99%, Sigma Aldrich) were used as precursors. In the synthesis of $CuCrO_2$ nanoparticles, firstly 4.65 g of $Cu(NO_3)_2 \cdot 2.5\,H_2O$ and 8 g of $Cr(NO_3)_3 \cdot 9\,H_2O$ were added together into 100 ml of deionized water and stirred for 1 h at room temperature on a magnetic stirrer. Then 8 g of NaOH was dissolved in the above solution by vigorous stirring for about 15 min. The final solution was then treated at 230 °C for 60 h under hydrothermal conditions. After cooling to room temperature, the precipitates were collected on a filter paper and washed with hydrochloric acid (1 M, 99%, Sigma Aldrich) and ethanol ($C_2H_5OH$, 96%, Sigma Aldrich) in sequence for four times to remove any contamination. The final product was dried in an oven for 12 h at 90 °C and stored under ambient conditions for further use.

### 2.3. *Preparation of ZnO-$CuCrO_2$ heterostructure*

ZnO-$CuCrO_2$ heterostructured photocatalysts were prepared by simply drop casting of the obtained $CuCrO_2$ nanoparticles dispersion on the heat treated ZnO fibres, as presented in Fig. 1. For this purpose, certain amount of the as-precipitated $CuCrO_2$ nanoparticles were sonicated in 2 ml of alcohol for 2 h at room temperature. Then, this dispersion was dropped on 50 mg of ZnO fibre pieces. During the preparation of ZnO-$CuCrO_2$ photocatalysts the amount of ZnO was kept constant. On the other hand, $CuCrO_2$ dispersions were prepared at different concentrations in order to obtain a series of ZnO-$CuCrO_2$ photocatalysts with different amount of $CuCrO_2$. For this study, ZnO fibres were wrapped with 0.5, 1.0 and 1.2 wt.% $CuCrO_2$. To avoid any inhomogeneity during the drop casting, at least five samples were prepared for each composition and the volume of the $CuCrO_2$ suspension remained constant. The heterostructured photocatalysts were first maintained under ambient conditions for 2 h, then heat treated at 400 °C for 1 h for the possibility of partial merging of two semiconductors via interdiffusion to form an interface.

### 2.4. *Characterization*

X-ray diffraction (XRD) analyses were used to identify the crystal structure of the electrospun ZnO fibres, as-precipitated $CuCrO_2$ nanoparticles and wrapped fibres. Measurements were performed via Bruker D8 Advance diffractometer operating at 40 kV and 40 mA. Patterns were obtained using $CuK_\alpha$ radiation with a wavelength of 0.154 nm in Bragg-Brentano mode at a scan speed of 2 °/min. The core-levels of all species at the surface of the samples were examined via high resolution X-ray photoelectron spectroscopy (XPS) using a Thermo Scientific $K_\alpha$ X-ray photoelectron spectrometer with monochromatic Al-$K_\alpha$ radiation. The size/diameter, crystallinity and morphology of the prepared samples and also the heterostructured photocatalysts were analysed using a JEOL JEM 2100F transmission electron microscope (TEM). The optical ab-

sorption was studied with UV-vis spectrophotometer VWR 3100-PC in the wavelength range of 300–650 nm at room temperature. For this purpose, a suspension of 12.5 mg of a sample in 20 ml of DI-water was firstly prepared by sonication. Then 4 ml of this aqueous suspension was further diluted in 50 ml of DI-water. The measurement of this suspension was performed in a standard quartz cuvette.

### 2.5. Photocatalytic properties

Photocatalytic activities of the pure and wrapped ZnO fibres were determined by performing degradation experiments with MB dye in aqueous solutions. Experiments were carried out in a custom made photocatalytic activity measurement system consisting of a water cooled reactor and light sources. Test suspensions (100 ml) were prepared using dye concentration of 10 mg/l and 50 mg of photocatalyst. Prior to light exposure, the suspensions were magnetically stirred in the dark for 60 min. All tests were performed in ambient air, without any additive for pH control and using a 250 W metal halide lamp (GE Lighting, ARC250/T/H/970/E40) which was 22 cm away from the suspension surface. At 15 min intervals, ~2 ml of the liquor was sampled, centrifuged and filtered through a 0.45 μm Teflon syringe filter to remove photocatalyst pieces. Then these filtrates were analysed by recording variations in the maximum absorption band (~663 nm for MB) using a VWR 3100-PC ultraviolet and visible spectrophotometer.

## III. Results and discussion

### 3.1. Structure of ZnO-$CuCrO_2$

XRD diffractograms of the ZnO fibres prepared with different $CuCrO_2$ content (0.0, 0.5, 1.0 and 1.2 wt.%) are shown in Fig. 2a. XRD patterns for the pure ZnO fibres and $CuCrO_2$ nanoparticles are also given for comparison. To the extent of the XRD detection limit, hexagonal wurtzite ZnO crystal structure (JCPDS: 36-1451) was the only phase that was detected for all heterostructured samples. No characteristic peaks were observed corresponding to $CuCrO_2$. This may be due to good dispersion and small quantities of the p-type particles. The sharp diffraction peaks for the pure fibres show high crystallinity. However, peak intensities of all wrapped samples are getting lower than that of the bare one which is due to the covering of the fibre surfaces with $CuCrO_2$ nanoparticles. Furthermore, peak broadening is observed for the wrapped ZnO fibres compared to the pure one. The effect of the $CuCrO_2$ addition on the broadening of diffraction peaks can be explained by the change in the crystallite size. The average crystallite size along the *c*-axis of the fibres was calculated by Scherrer's equation using the XRD line broadening method:

$$D = \frac{0.9\lambda}{\beta \cdot \cos\theta} \tag{1}$$

where $\lambda$ is the X-ray wavelength for $CuK_\alpha$, $\beta$ is the full width at half maximum (FWHM) of the diffraction line and $\theta$ is the Bragg angle of 0002 diffraction peak. The $CuCrO_2$ particles probably inhibit the particle growth during the heat treatment at 400 °C for 1 h performed after drop casting. Thus, the modified ZnO fibres are constituted of particles with smaller crystallite size than that in the pure sample, as listed in Table 1.

Detailed structural information can be obtained from the enlarged XRD patterns (for $2\theta$ between 31° and 37°) shown in Fig. 2b and data given in Table 1. It is interesting to note that with increasing $CuCrO_2$ amount, the

**Table 1. XRD crystallite size (*D*), position of ZnO 0002 peak ($2\theta$) and lattice parameters (*c*) for pure and $CuCrO_2$ wrapped ZnO fibres with different $CuCrO_2$ contents**

| $CuCrO_2$ [wt.%] | *D* [nm] | $2\theta$ [°] | *c* [Å] |
|---|---|---|---|
| 0 | 29.98 | 34.24 | 5.198 |
| 0.5 | 23.38 | 34.26 | 5.184 |
| 1.0 | 20.17 | 34.27 | 5.178 |
| 1.2 | 20.78 | 34.39 | 5.104 |

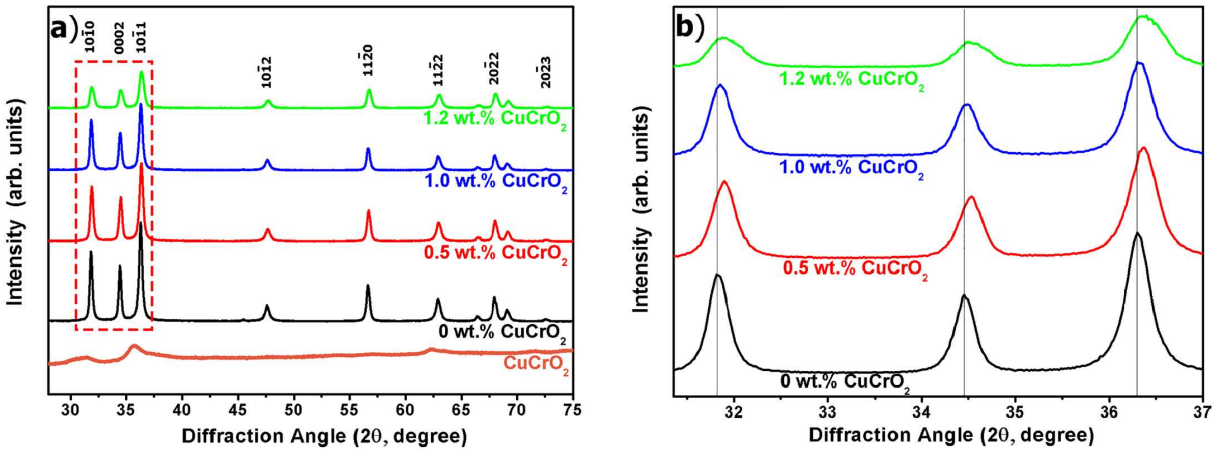


**Figure 2. XRD patterns (overview (a) and enlarged region (b)) of pure and $CuCrO_2$ wrapped ZnO fibres with different $CuCrO_2$ contents**

diffraction line position of ZnO shifts towards higher $2\theta$ degrees. This shift suggests that the presence of $CuCrO_2$ nanoparticles changes the lattice parameter ($c$) of the ZnO fibres, as listed in Table 1. There is a lattice constriction with increasing $CuCrO_2$ amount. Lattice parameter narrowing trend may be explained by substitutional incorporation of Cu/Cr ions into ZnO crystal [47]. As a $CuMO_2$ type delafossite, in the $CuCrO_2$ crystal structure, Cu and Cr ions have monovalent and trivalent states, respectively. In addition, for the same coordination number, ionic radius of $Zn^{2+}$, $Cu^{+}$ and $Cr^{3+}$ are 0.74, 0.77 and 0.61 Å, respectively [48]. Therefore, the observed lattice parameter contraction is expected mainly as a result of replacement of $Zn^{2+}$ with $Cr^{3+}$ ions. However, to protect charge balance, some part of $Cu^{+}$ ions should be substitutionally sitting in the ZnO lattice.

### 3.2. *Chemical properties of ZnO-$CuCrO_2$*

The chemical composition and ionic states of the elements for the pure and 1.0 wt.% $CuCrO_2$ wrapped ZnO fibres were investigated by XPS analyses. Figure 3a shows typical wide scan spectra of the fibres. In the pure fibre spectrum, Zn, O and C main element peaks were observed. However, survey spectrum of the wrapped ZnO fibres with 1.0 wt.% $CuCrO_2$ shows additional Cu and Cr signals which can be attributed to the successful wrapping of the pure ZnO fibres with $CuCrO_2$ nanoparticles. The detected C is related to trace amount of removable polymer during the heat treatment or adsorption of organic contaminants during handling. All binding energies were adjusted for the charge shift using the C(1$s$) peak of graphitic carbon located at 284.6 eV [49].

For characterizing detailed chemical states, high resolution XPS spectra of the Zn(2$p$), O(1$s$), Cu(2$p$) and

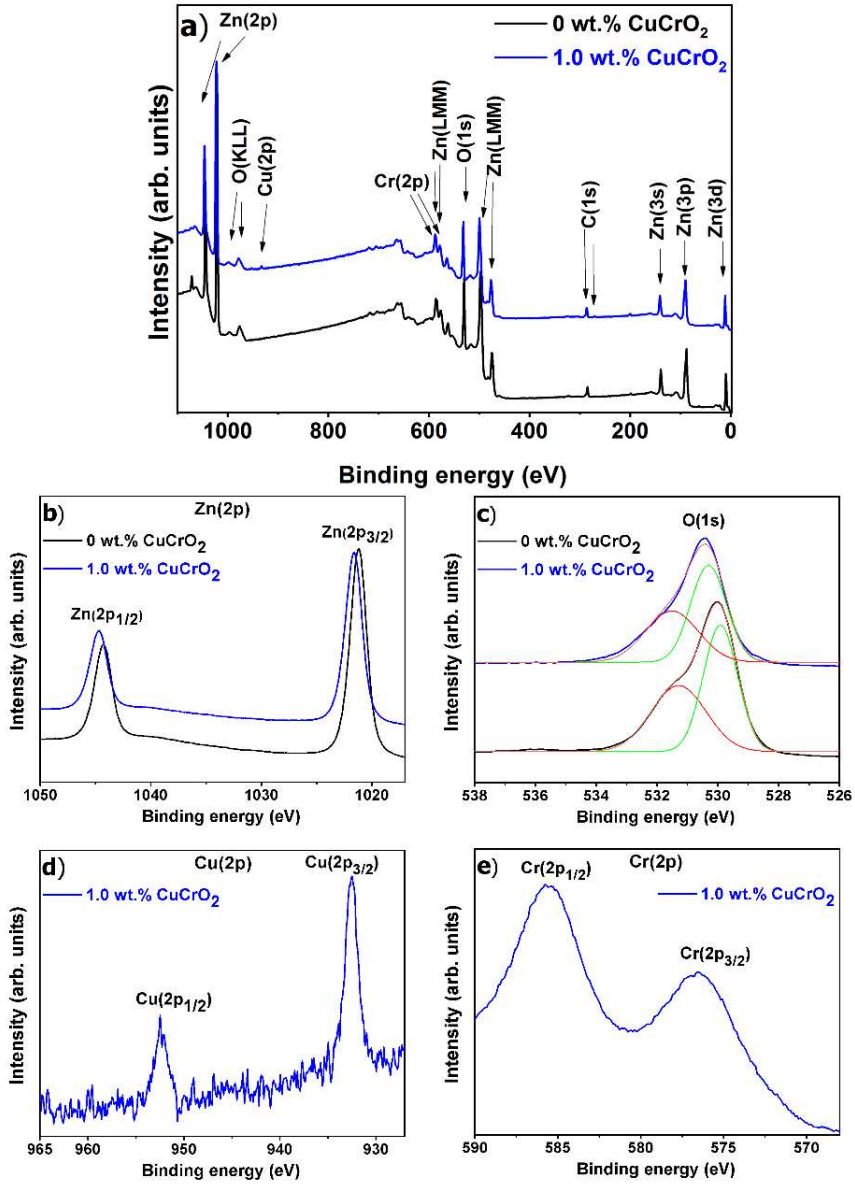


**Figure 3. XPS spectra for pure and $CuCrO_2$ wrapped ZnO fibres with different $CuCrO_2$ contents - a) survey analyses, and high resolution regional spectra of: b) Zn(2$p$), c) O(1$s$), d) Cu(2$p$) and e) Cr(2$p$) signals**

Cr(2$p$) core levels were analysed and shown in Fig. 3b-e, respectively. For the pure ZnO fibres, the corresponding Zn(2$p$) high resolution spectra (Fig. 3b) exhibits two peaks (1021.10 and 1044.27 eV) originating from the strong spin orbit coupling of Zn [50]. O(1s) core level for the pure ZnO fibres is a combination of two different Gaussian peaks (Fig. 3c). The first peak located at 530.9 eV can be correlated with the lattice oxygen ions in the ZnO lattice and the second one at 532.32 eV is attributed to chemisorbed oxygen, such as surface hydroxyl groups [51]. Zn(2$p$) and O(1$s$) binding energies of the pure fibres match with that of the stoichiometric ZnO [47]. Compared to the Zn(2$p$) core levels of the pure ZnO fibres, the $CuCrO_2$ wrapped sample showed a little shift to the higher binding energy (Zn($2p_{3/2}$): 1021.58 eV and Zn($2p_{1/2}$): 1044.68 eV) which indicates modification of the ZnO surface with $CuCrO_2$. Furthermore, the binding energies of the O(1$s$) components of the wrapped fibres are also slightly higher than that of the pure sample (531.34 and 532.76 eV). These binding energy differences can be explained with the variation of the chemical environment of ions due to the change of the electronegativity differences of the bonds formed between oxygen and cation ions. In the case of the pure fibres, all bonds are formed between $Zn^{2+}$ and $O^{2-}$ ions. However, in the wrapped fibre structure, the cation can be $Zn^{2+}$, $Cu^{+}$ or $Cr^{3+}$ which results in different electronegativity values than the Zn–O bond and thus different valence electron density occurs. Similar observations were also reported for Cu- and Co-doped ZnO nanostructures [5,47].

XRD results suggest that some part of $CuCrO_2$ cations are substitutionally incorporated at $Zn^{2+}$ lattice sites of ZnO. To figure out the presence of Cr ions in the 1.0 wt.% $CuCrO_2$ wrapped ZnO fibres, the high resolution Cr(2$p$) XPS core level spectrum was measured (Fig. 3d). There are two strong peaks centred at 576.5 and 585.5 eV which can be attributed to the binding energies of Cr($2p_{3/2}$) and Cr($2p_{1/2}$), respectively [52], confirming the presence chromium in the trivalent state ($Cr^{3+}$).

It is well known that XPS is a highly effective technique to distinguish states of Cu due to different features of Cu(2$p$) signals. Sharp and well-defined signals of Cu($2p_{3/2}$) and Cu($2p_{1/2}$) located at 932.6 and 952.5 eV are observed in the metallic Cu ($Cu^0$). However, slightly narrower peak widths at nearly the same binding energy values is observed in the monovalent state of Cu ($Cu^{+}$). In addition, divalent Cu ions ($Cu^{2+}$) exhibit broad two peaks located at nearly 1 eV higher binding energy than that of $Cu^0$ and $Cu^{+}$ (Cu($2p_{3/2}$) at 934.6 eV and Cu($2p_{1/2}$) at 954.3 eV). Furthermore, unlike $Cu^0$ and $Cu^{+}$, $Cu^{2+}$ produces strong Cu(2$p$) satellite peaks appearing at higher binding energy showing the presence of Cu 3$d$ hole states [53]. From Fig. 3e presence of two Cu($2p_{3/2}$) and Cu($2p_{1/2}$) peaks is observed at 932.44 and 952.44 eV, respectively. The position and shape of Cu signals indicate that Cu is mainly in the $Cu^{+}$ ionic state. Therefore, according to the high resolution Cu XPS spectra, substitutional incorporation of $CuCrO_2$ in $Cu^{+}$ form into fibre structure is observed at vicinity of interface, whereas wrapped $CuCrO_2$ is found again in $Cu^{+}$ form near surface. These results are in agreement with the XRD data.

### 3.3. Microstructure of ZnO-$CuCrO_2$

Figure 4 shows TEM micrograph of the heat-treated ZnO fibres. It confirms the presence of a representative typical morphology for electrospun ceramic fibres. As seen from this image, the ZnO fibres have dense and continuous wire-like morphology. According to the measurements performed using SEM images (inset in Fig. 4), the average diameter of the annealed fibres was determined as 172 ± 42 nm. The TEM micrograph given here also reveals that the fibres exhibit a size distribution in terms of the fibre diameter. The image shows two overlapped fibres with diameters of 90 and 140 nm. The selected area electron diffraction (SAED) pattern given as an inset implies the polycrystalline nature of the fibres. The visible lattice fringes observed in the high resolution TEM (HR-TEM) image has also proved the formation of wurtzite phase (lower left of Fig. 4). The distance between neighbouring planes is determined as 2.63 Å which matches with the interplanar spacing of (0002) planes of wurtzite ZnO. SAED pattern (Fig. 4) was recorded from the crystal mentioned above, showing its single crystalline nature. Thus, the polycrystalline ZnO fibres are composed of randomly oriented and attached single crystals of wurtzite ZnO phase ($d_{av} \leq 50$ nm). This finding is in well accordance with the crystallite size calculated using the Scherrer equation from the XRD pattern of the pure ZnO fibres.

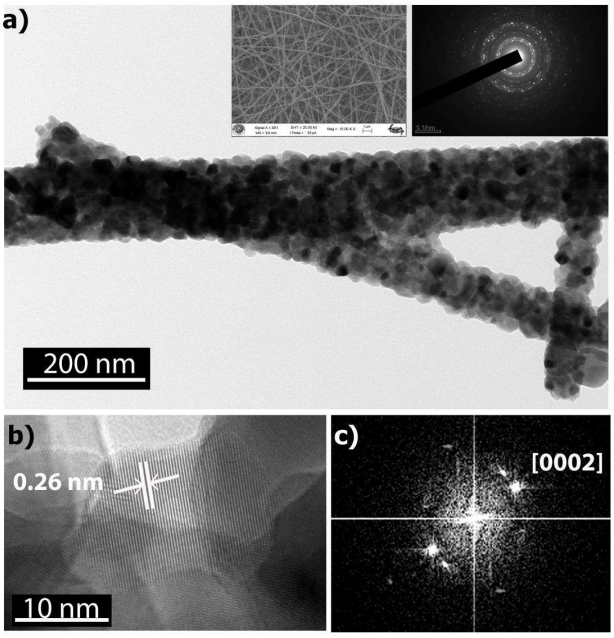


**Figure 4. TEM image of pure ZnO fibres - insets are SEM micrograph and SAED pattern (a), HR-TEM image (b) and SAED pattern (c) of a single ZnO nanoparticle**

Similarly, Fig. 5 presents TEM data of the as-precipitated $CuCrO_2$ nanoparticles. The TEM image reveals the nanoparticulate nature and typical plate-like morphology of the hydrothermally synthesized $CuCrO_2$ precipitates. As revealed in previous studies, hydrothermal synthesis led to the formation of single crystal $CuCrO_2$ precipitates in quasi-hexagonal nano-plate morphology with an average diameter of about 10–20 nm [46,54]. The average diameter and thickness of the nanoparticles for the current study were determined by measuring the distance parallel and normal to (00l) faces of 50 randomly distributed individual particles and found to be 12 and 5 nm, respectively. HR-TEM image of a randomly selected as-prepared $CuCrO_2$ nanoparticle is given in Fig. 5b. The interplanar distance determined as 0.285 nm matches with the (006) interplanar spacing of $CuCrO_2$ structure and corresponds to the distance between the Cu planes in the $CuCrO_2$. SAED pattern of the selected $CuCrO_2$ nanoparticle (Fig. 5c) indicates that the $CuCrO_2$ crystals grow mainly through six faces with a high growth rate of {012} and agrees with the *d* spacing of (006).

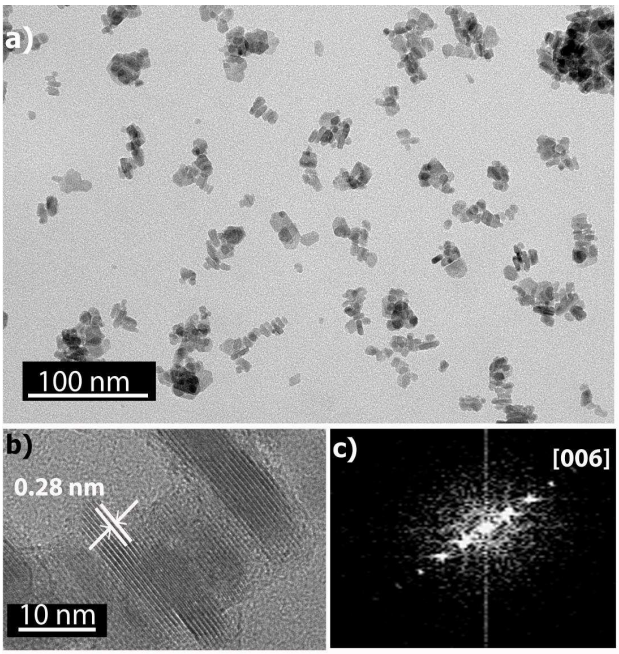


**Figure 5. TEM image of the $CuCrO_2$ nanoparticles (a), HR-TEM image (b) and SAED pattern (c) of a single $CuCrO_2$ nanoparticle**

TEM was also used to investigate the microstructural features of the $CuCrO_2$ wrapped ZnO fibres. Figure 6 shows low and high resolution TEM images of the 1.0 wt.% $CuCrO_2$ wrapped ZnO fibre photocatalyst after annealing at 400 °C for 1 h. Figure 6a presents the formation of $CuCrO_2$-ZnO composite structure via random accumulation of the nanoparticles on fibres (marked with white dashed lines). This is an expected result for the ZnO-$CuCrO_2$ heterostructure achieved via drop casting of the $CuCrO_2$-alcohol dispersion on the ZnO fibres. During this step, highly porous structure of fibres probably leads to quick propagation of alcohol due to capillary forces. The spreading of the liquid phase also carries the nanoparticles and finally deposits them randomly on fibre surfaces which yields a typical morphology as shown in Fig. 6b. In addition, the grain growth of $CuCrO_2$ nanoparticles during the preparation of heterostructured photocatalyst might be recognised when comparing their size to the size of the as-precipitated $CuCrO_2$ nanoparticles mentioned above. The increase in size is a result of the solid state diffusion as evidenced by the clear neck formation between the nanoparticles (indicated by black arrow in Fig. 6b).

As a consequence, some particles reached almost the equilibrium shape of the delafossite $CuCrO_2$ crystals as discussed previously in the literature [55,56], i.e. hexag-

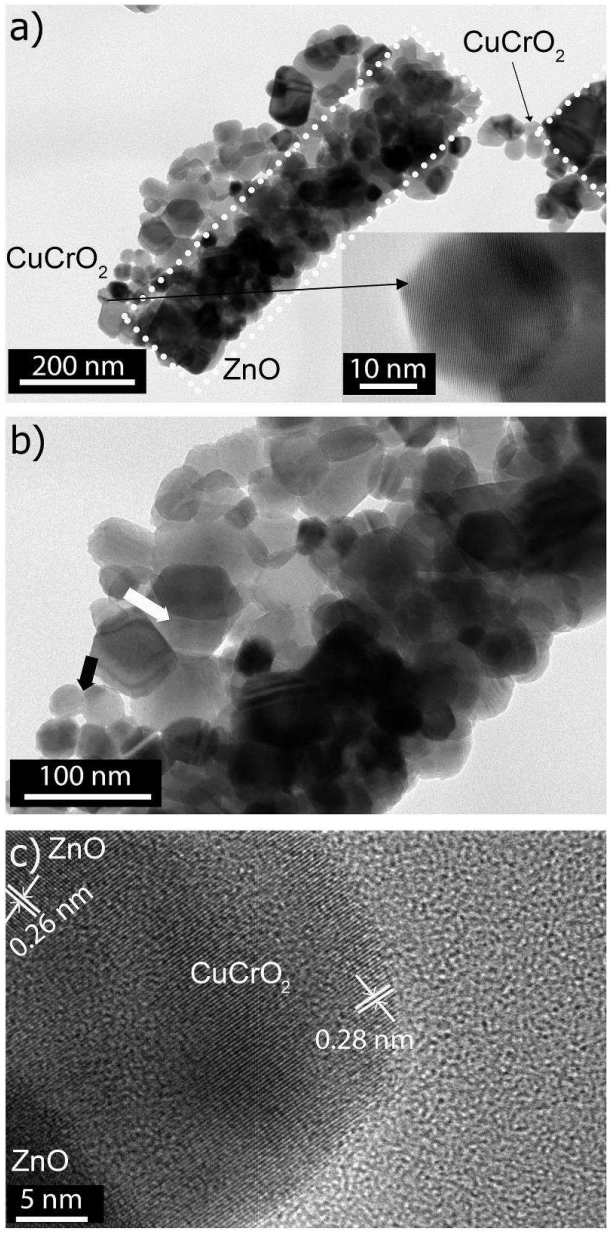


**Figure 6. TEM image of 1.0 wt.% $CuCrO_2$ wrapped ZnO fibres - inset is HR-TEM image (a), higher magnification TEM image (b) and HR-TEM image of p-n heterojunction interface (c)**

onal nano-plate morphology (pseudosix-fold symmetry) with size of about 70 nm (indicated by white arrow in Fig. 6b). Figure 6c shows the formation of an interface between the ZnO fibre and a $CuCrO_2$ nanoparticle. Two types of lattice fringes can be observed from this high resolution image. The interplanar spacing of 0.28 and 0.26 nm match with (006) planes of $CuCrO_2$ and (0002) planes of wurtzite ZnO crystal, respectively. In addition, the continuity of the lattice fringes at the interface between the ZnO crystal and $CuCrO_2$ nanoparticle may prove the formation of p-n heterojunction [31]. Furthermore, the formation and observation of an interface between the two phases also corroborate the inferred results from the XRD and XPS data on peak position shift as a result of partial interdiffusion between $Zn^{2+}$ and $Cu^{+}$ and $Cr^{3+}$ ions.

### 3.4. Optical properties of ZnO-$CuCrO_2$

Optical properties of the pure and wrapped ZnO fibres were investigated using a UV-vis spectrophotometer between 300–650 nm wavelength to reveal the effects of $CuCrO_2$ on the optical properties of the heterostructured photocatalyst. The optical absorption spectra of the prepared samples as a function of $CuCrO_2$ amount are presented in Fig. 7. The corresponding direct band-gaps of the samples are also given as insets in Fig. 7. The wavelength of the absorption edge was estimated by extrapolating the horizontal and rising portions of the curves and defining the intersection as the wavelength of the edges. Ding *et al.* [57] observed two distinct absorption peaks for ZnO nanorod array – $CuAlO_2$ laminar film heterojunctions, which correspond to the absorption edge of ZnO and $CuAlO_2$ components. For the current study, only one single peak was observed which corresponds to the absorption edge of ZnO. This may be due to the very low amount of the delafossite phase which was only up to 1.2 wt.%. As shown in Fig. 7, the absorption edge of the pure ZnO fibres (375 nm) shows a red shift to the higher wavelengths for the wrapped samples. However, the red shift does not increase monotonously with the amount of $CuCrO_2$, as can be seen by comparing the absorbance peak positions of the 0.5 wt.% $CuCrO_2$ wrapped sample and the others. As suggested by XRD and XPS measurements, substitution of $Cu^{+}$ and $Cr^{3+}$ ions into ZnO lattice occurs during 1 h of the heat treatment at 400 °C. Such impurity incorporation might induce defects in the lattice of wurtzite ZnO, resulting in a shift of the absorption edge in comparison to the pure ZnO. Thus, absorption edge change gives information about the electronic band structure change of the ZnO due to the doping [5,47]. Theoretically, the wavelength of the absorption edge should increase with the increase in the amount of $CuCrO_2$ in the heterostructured samples. However, among the prepared samples, the highest absorption edge was observed for the 0.5 wt.% $CuCrO_2$ wrapped ZnO fibres. This might be related to the preferential incorporation of $Cr^{3+}$ and $Cu^{+}$ ions into the ZnO lattice. For the sample wrapped with 0.5 wt.% $CuCrO_2$, the copper ions may have diffused in a relatively higher amount then the chromium ions resulting in the narrowest $E_g$. With the increase in $CuCrO_2$ amount, both chromium and copper ions might have diffused into ZnO, but amount of diffused chromium might be relatively higher than that of the copper. Although there are contradictory results presented in the literature on the effect of Cr doping on the optical properties of ZnO, in many recent study it was shown that Cr incorporation promotes blue shift, contrary to the Cu incorporation, in the absorption edge of ZnO [58,59]. Thus, the shift in the wavelength edge for the current study probably depends on the relative amount of $Cr^{3+}/Cu^{+}$ incorporation into ZnO host lattice. This also explains why the lowest absorption edge wavelength occurs for the 1.2 wt.% $CuCrO_2$ containing sample. Despite all, the red shift of absorption edge to the higher wavelengths compared to the pure fibres is an indication that the wrapped samples can also absorb light in the higher wavelengths, and therefore may utilize more of the spectrum for the photocatalytic reactions.

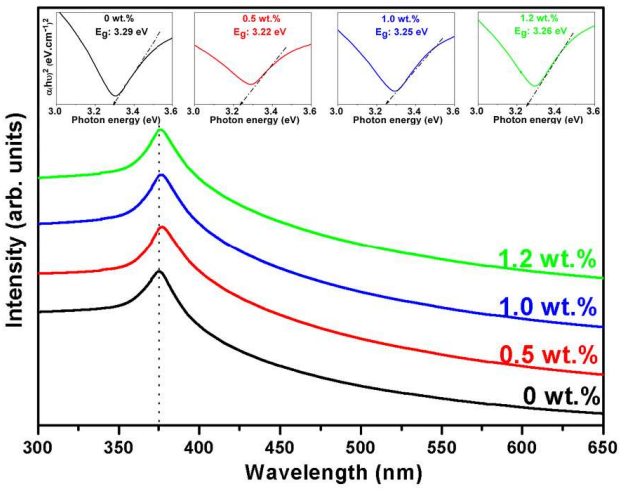


**Figure 7. The UV-vis spectra of pure and the $CuCrO_2$ wrapped ZnO fibres with different $CuCrO_2$ contents (insets show plots of $(\alpha h\nu)^2$ as a function of photon energy)**

Absorption edge shift also means a change in the direct band gap energies ($E_g$) of the samples. The $E_g$ of the pure ZnO fibre and heterostructured samples were estimated by plotting the absorption coefficient ($\alpha$) photon energy graph ($h\nu$) and extrapolating the straight-line portion of this plot to the $h\nu$ axis as shown in insets in Fig. 7. For the pure ZnO nanofibers $E_g$ was determined as 3.29 eV. This value is close to the reported value of ZnO (3.34 eV) [47]. $E_g$ of the pure $CuCrO_2$ was reported as 3.0 eV [46] and the difference in the $E_g$ values of the pure ZnO and $CuCrO_2$ causes photoresponse observed in Fig. 7 as a red shift in the absorption edge [60]. For the heterostructured samples, band gap values were obtained as 3.22, 3.25 and 3.26 eV for 0.5, 1.0 and 1.2 wt.% $CuCrO_2$ containing samples, respectively. This finding shows that the band gap of the ZnO-$CuCrO_2$ heterostructured samples fall in between that of the pure

ZnO and $CuCrO_2$. This is due to the individual contribution of each crystalline phase, i.e. $CuCrO_2$ and ZnO to $E_g$ in the composite structure. In summary, considering the results of XRD, XPS, TEM and UV-vis spectra, it can be concluded that the cations from $CuCrO_2$ were incorporated into the ZnO lattice up to some extent and two types of semiconductors form p-n heterojunctions. Therefore, this architecture might exhibit better photocatalytic ability compared to the pure ZnO fibres.

### 3.5. *Photocatalytic properties of ZnO-CuCrO2*

The photocatalytic activities of the heterostructured photocatalysts with different amount of $CuCrO_2$ were evaluated via the decomposition of MB dye under the irradiation of UV-visible light. Further, the photodegradation behaviour of MB in the absence of the catalyst was checked under the same experimental conditions. As to compare, the photocatalytic degradation of MB over the pure ZnO fibres was recorded and used as a reference. The degradation efficiency of the samples was defined as $(C_0 - C_t)/C_0$, where $C_0$ and $C_t$ were the initial and remaining concentration of MB after exposure to light for time $t$, respectively.

Figure 8 shows the photocatalytic performances of the pure and $CuCrO_2$-ZnO heterostructures as a function of UV-visible light exposure time. It is obvious that there is no significant degradation of MB occuring after 2 h in the absence of the catalyst. This indicates that the decomposition of MB under UV-visible light irradiation can be ignored. For catalyst loaded experiments, the dye degraded for all samples. As seen from the shape of the curves, the absorbance of the dye decreased exponentially as a function of time. The degradation efficiency of MB after 1 h of light exposure was about 83.5% in the case of the pure ZnO fibres. Similarly, the degradation efficiency reached 87.3 and 93.4% for the 0.5 and 1.0 wt.% $CuCrO_2$ wrapped samples, respectively. On the other hand, the amount of decomposition was

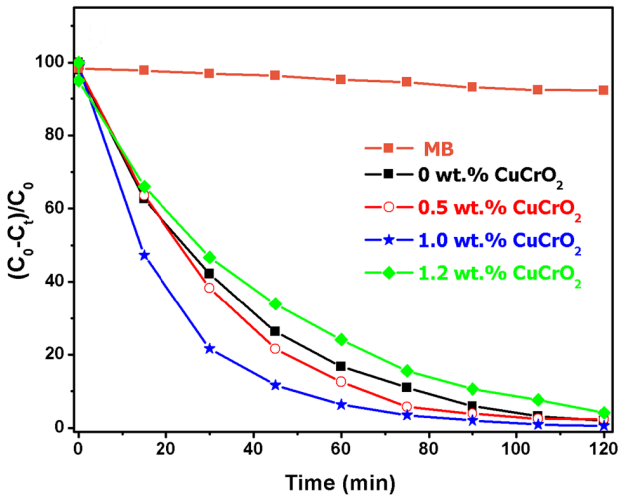


**Figure 8. Temporal profile of MB degradation of pure and $CuCrO_2$ wrapped ZnO fibres with different $CuCrO_2$ contents under UV-visible light illumination**

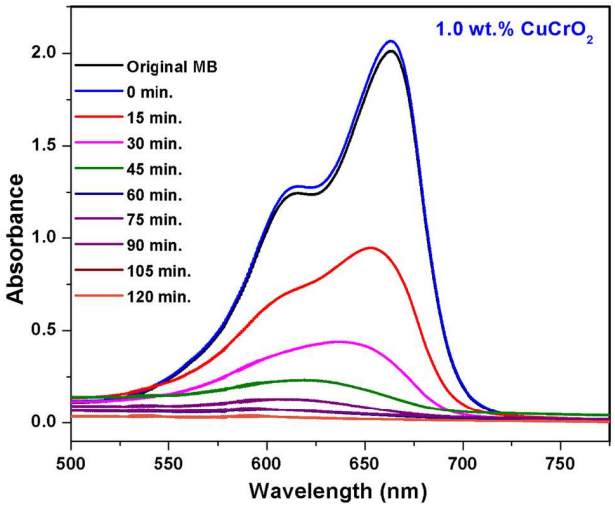


**Figure 9. Real-time UV-vis absorption spectra of the photodegradation of MB solutions containing 1 wt.% $CuCrO_2$ wrapped ZnO fibres**

decreased for the sample prepared by using 1.2 wt.% $CuCrO_2$. The degradation efficiency of MB after 1 h for this sample was 76.2%. While the amount of ZnO catalyst was kept constant in all experiment, the observed difference in the photocatalytic activity of the samples can be attributed to the presence of $CuCrO_2$. This finding shows that the ZnO-$CuCrO_2$ heterostructures have higher photocatalytic activity compared to that of the pure ZnO up to a certain amount of $CuCrO_2$ addition. For the current study, the limit of $CuCrO_2$ amount was identified as 1.0 wt.%. The absorbance spectra of MB aqueous solutions in the presence of the 1.0 wt.% $CuCrO_2$ wrapped ZnO fibres are given in Fig. 9. It can be seen that the absorbance peak appeared at 663 nm disappears completely after 120 min light irradiation. It is also worth to mention that this sample degraded almost 50% of the dye within the first 15 min. Due to too weak adsorption of dye molecules on the $CuCrO_2$-wrapped ZnO fibres, the observed photodegradation can only be originated from heterostructured photocatalyst. Moreover, absorbance spectra revealed that the maximum absorbance peak showed a blue shift from 663 to 638 nm after 30 min of irradiation. This shift was generally observed during the photocatalytic decomposition of methylene blue on conventional semiconductor photocatalyst and named as hypochromic effect [60].

The photocatalytic ability of the prepared $CuCrO_2$ wrapped ZnO fibres was further examined by evaluating the decomposition rates of dye molecules under the UV-visible light illumination. The kinetic linear simulation curves for the degradation of MB reveals that the decomposition reactions followed a Langmuir-Hinshelwood apparent first-order kinetics model [62]. When the initial concentration ($C_0$) is low as in the current study ($C_0$ = 10 mg/l), apparent first-order model equation ($\ln(C_t/C_0) = k_{app} \cdot t$) can be used to determine the apparent first-order rate constant [63,64]. In this respect, the values of $\ln(C_t/C_0)$ for all samples were plot-

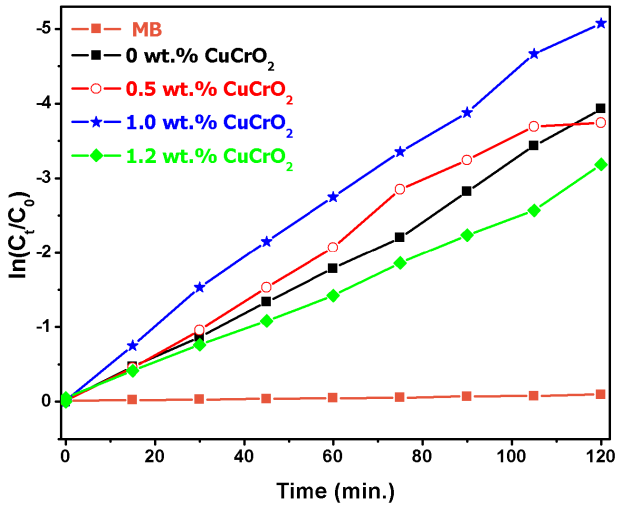


**Figure 10. The pseudo first-order kinetics of MB dye degradation for the pure and $CuCrO_2$ wrapped ZnO fibres with different $CuCrO_2$ contents**

ted as a function of the irradiation time and presented in Fig. 10. According to the results of the current study, the 1.0 wt.% $CuCrO_2$ wrapped ZnO fibre catalyst clearly presented much better photocatalytic activity compared to the pure ZnO fibres. Furthermore, the degradation rate of the MB dye in the presence of the ZnO-$CuCrO_2$ catalysts increased up to the 1.0 wt.% $CuCrO_2$ addition and then decreased. It is clear that the samples exhibit a linear behaviour. Thus, the reaction rate constants ($k$) were estimated from the slope of these plots as a function of $CuCrO_2$ amount in the photocatalysts. The reaction rate constants were obtained as 0.032, 0.038, 0.043 and 0.025 $min^{-1}$ for the pure and 0.5, 1.0 and 1.2 wt.% $CuCrO_2$ wrapped ZnO fibres, respectively. According to these results, $k$ values of the wrapped samples up to 1.0 wt.% $CuCrO_2$ are almost 30% higher than that of the pure ZnO fibres. However, in the case of the sample with 1.2 wt.% $CuCrO_2$, $k$ value and photocatalytic activity decreased significantly due to the hindering of the light by the excess $CuCrO_2$ particles. Similar behaviour was also observed for $CuCrO_2$ coated $TiO_2$ nanorods and attributed to the fading of the absorption of light by $TiO_2$ nanorods in the case of too much coverage on the surfaces [31]. The photocatalytic activity order presented here is well consistent with the activity mentioned above. Further, these results show both that the $CuCrO_2$ addition greatly improved the photocatalytic performance of the ZnO fibres and that 1.0 wt.% $CuCrO_2$ is the optimal content for $CuCrO_2$-ZnO heterostructures.

Based on the above experimental results, the increase in the photocatalytic activity of the pure fibres may be discussed depending on more than a single factor. The incorporation of $Cr^{3+}$ and $Cu^{+}$ cations into ZnO host lattice and the formation of a p-n heterojunction have a common effect on the red shift of the absorption edge, increase in the absorption amount, blue shift of the band-gap, and more efficient photo-generated charge carrier separation. For the first factor, the incorporation of cations with different radii and valence into ZnO lattice led to the shift of the absorption edge toward visible light, the increase in the absorption for all wavelengths and narrowing of the band gap after heterostructuring which are similar to doping of ZnO with transition metals, as discussed previously. For the second factor, the formation of the p-n heterojunctions contributed to the decrease in the recombination rate of charge carriers. A proposed mechanism and a representative schematic illustration for the enhanced photocatalytic activity of the n-type ZnO/p-type $CuCrO_2$ heterojunction is presented in Fig. 11. It had been reported that the ionization energy of $CuCrO_2$ and ZnO were 5.25 and 7.67 eV, respectively [63,65]. For the as-prepared $CuCrO_2$ nanoparticles and ZnO fibres, band gaps were determined as 3.06 and 3.29 eV, respectively. Further, the work functions were reported as 5.23 eV for $CuCrO_2$ and 5.2 eV for ZnO [63,65]. While the Fermi energy level of ZnO was higher than that of $CuCrO_2$, when these two formed a heterojunction, the electron transfer could occur from ZnO to $CuCrO_2$. Meanwhile, the holes could transfer from $CuCrO_2$ to ZnO until the equilibrium is achieved between $CuCrO_2$ and ZnO [35]. As a result, the p-n heterojunction leads to the formation of positively and negatively charged regions in n-ZnO and p-$CuCrO_2$, respectively. This internal electric field improves the separation of photo-generated charge carriers [66]. Under the light irradiation, photo-excited holes in valance band of ZnO can now migrate to valence band of $CuCrO_2$. In a similar fashion, photo-excited electrons from the conduction band of $CuCrO_2$ can migrate to the conduction band of ZnO. These transitions are the main reason for the decrease in the recombination rate of $e^{-}$–$h^{+}$ pairs [67]. Thus, the photocatalytic activity of the composite structure enhances. In terms of the degradation process, now the photo-excited $e^{-}$ accumulated on the conduction band of ZnO can react more efficiently with the $O_2$ and generate $O_2^{-}$. Meanwhile, the $h^{+}$ on the valence band of $CuCrO_2$ can now oxidize $H_2O$ or $OH^{-}$ into hydroxyl radicals [68,69], as shown in Fig. 11.

In brief, it is clear that the formation of p-n heterojunction interfaces and the decline of band gap energy due to the substitutional incorporation of $Cr^{3+}$ and $Cu^{+}$ ions concurrently suppressed the recombination rate and

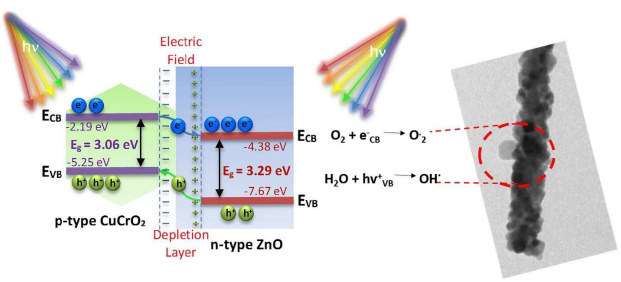


**Figure 11. Schematic illustration of the energy band structure and electron-hole pair separation in the $CuCrO_2$-ZnO p-n heterojunctions**

enhanced the transfer of charge carriers, respectively. As a result, this synergistic effect improves the photocatalytic efficiency of heterostructured photocatalyst. Therefore, the proposed p-n heterojunction system can provide useful insights for the large-scale production of efficient ZnO-$CuCrO_2$ visible light photocatalyst systems.

## IV. Conclusions

In summary, p-n type $CuCrO_2$-ZnO heterojunction photocatalyst was prepared for the first time via wrapping of hydrothermally synthesized $CuCrO_2$ nanoparticles on electrospun ZnO fibres. The effects of $CuCrO_2$ addition on the microstructure, chemical, optical and photocatalytic properties of ZnO fibres were systematically studied. Detailed analysis of p-n heterojunctions was performed by XRD, XPS, TEM and optical property measurements. It was found that $CuCrO_2$ wrapping caused a shift in the XRD peak positions of wurtzite ZnO to the higher diffraction angles showing a reduction in the lattice parameter ($c$). The Cu($2p$) and Cr($2p$) core level XPS signal positions indicated that both $Cu^+$ and $Cr^{3+}$ are substitutionally incorporated into ZnO crystal structure through the interface of the p-n heterojunctions. TEM and HR-TEM analyses showed that the p-n heterostructure was successfully formed between ZnO-$CuCrO_2$ nanostructures. The $CuCrO_2$ wrapping also caused a decrease in the band gap energy of ZnO fibres as demonstrated with the change in the absorption edge to longer wavelengths. Furthermore, the photocatalytic performances of the heterojunctions were examined by degrading MB under UV-visible light irradiation. With 93.4% degradation efficiency after 1 h, the 1 wt.% $CuCrO_2$ was determined to be optimal content for the ZnO-$CuCrO_2$ p-n heterojunction system. This enhanced photocatalytic activity is originating from a synergistic action of: i) formation of p-n heterojunctions and ii) the effective carrier separation by ionic incorporation of p-type oxide cations. We believe that this report on the preparation of $CuCrO_2$ nanoparticles-ZnO fibres with p-n type heterojunctions and the presented results provide a simple and effective route to achieve composite structured photocatalysts with enhanced photocatalytic behaviour.

**Acknowledgements:** The authors wish to thank İsmail Cihan Kaya for his support in the synthesis of $CuCrO_2$ nanoparticles.

## References

1. T. Zhang, X. Wang, X. Zhang, "Recent progress in $TiO_2$-mediated solar photocatalysis for industrial wastewater treatment", *Int. J. Photoenergy*, **2014** (2014) 607954.
2. M.R. Hoffmann, S.T. Martin, W. Choi, D.W. Bahnemann, "Environmental applications of semiconductor photocatalysis", *Chem. Rev.*, **95** [1] (1995) 69–96.
3. Y. Qu, X. Duan, "Progress, challenge and perspective of heterogeneous photocatalysts", *Chem. Soc. Rev.*, **42** [7] (2013) 2568–2580.
4. M. Samadi, M. Zirak, A. Naseri, E. Khorashadizade, A.Z. Moshfegh, "Recent progress on doped ZnO nanostructures for visible-light photocatalysis", *Thin Solid Films*, **605** (2016) 2–19.
5. O.A. Yildirim, H. Arslan, S. Sönmezoğlu, "Facile synthesis of cobalt-doped zinc oxide thin films for highly efficient visible light photocatalysts", *Appl. Surf. Sci.*, **390** (2016) 111–121.
6. Ö.A. Yıldırım, H.E. Unalan, C. Durucan, "Highly efficient room temperature synthesis of silver-doped zinc oxide (ZnO:Ag) nanoparticles: Structural, optical, and photocatalytic properties", *J. Am. Ceram. Soc.*, **96** [3] (2013) 766–773.
7. C. Busuioc, A. Evanghelidis, M. Enculescu, I. Enculescu, "Optical and photocatalytic properties of electrospun ZnO fibers", *Digest J. Nanomater. Biostruct.*, **10** (2015) 957–965.
8. Z. Wang, Y. Liu, B. Huang, Y. Dai, Z. Lou, G. Wang, X. Zhang, X. Qin, "Progress on extending the light absorption spectra of photocatalysts", *Phys. Chem. Chem. Phys.*, **16** [7] (2014) 2758–2774.
9. O.M. Ishchenko, V. Rogé, G. Lamblin, D. Lenoble, "$TiO_2$- and ZnO-based materials for photocatalysis: Material properties, device architecture and emerging concepts", pp. 3–30 in *Semiconductor Photocatalysis-Materials, Mechanisms and Applications*, InTech Open, Croatia, 2016.
10. S.A. Ansari, M.H. Cho, "Highly visible light responsive, narrow band gap $TiO_2$ nanoparticles modified by elemental red phosphorus for photocatalysis and photoelectrochemical applications", *Sci. Reports*, **6** (2016) 25405.
11. S. Dong, J. Feng, M. Fan, Y. Pi, L. Hu, X. Han, M. Liu, J. Sun, J. Sun, "Recent developments in heterogeneous photocatalytic water treatment using visible light-responsive photocatalysts: A review", *RSC Advances*, **5** [19] (2015) 14610–14630.
12. S. Anandan, Y. Ikuma, K. Niwa, "An overview of semiconductor photocatalysis: modification of $TiO_2$ nanomaterials", *Solid State Phenom.*, **162** (2010) 239–260.
13. Y. Peng, S. Qin, W.-S. Wang, A.-W. Xu, "Fabrication of porous Cd-doped ZnO nanorods with enhanced photocatalytic activity and stability", *CrystEngComm*, **15** [33] (2013) 6518–6525.
14. J. Chiou, S. Ray, H. Tsai, C. Pao, F. Chien, W. Pong, C. Tseng, J. Wu, M.-H. Tsai, C.-H. Chen, "Correlation between electronic structures and photocatalytic activities of nanocrystalline-(Au, Ag, and Pt) particles on the surface of ZnO nanorods", *J. Phys. Chem. C*, **115** [6] (2011) 2650–2655.
15. A. Di Mauro, M. Zimbone, M. Scuderi, G. Nicotra, M.E. Fragalà, G. Impellizzeri, "Effect of Pt nanoparticles on the photocatalytic activity of ZnO nanofibers", *Nanoscale Res. Lett.*, **10** [1] (2015) 484.
16. D. Lin, H. Wu, R. Zhang, W. Pan, "Enhanced photocatalysis of electrospun Ag-ZnO heterostructured nanofibers", *Chem. Mater.*, **21** [15] (2009) 3479–3484.
17. Q. Wang, B. Geng, S. Wang, "ZnO/Au hybrid nanoarchitectures: wet-chemical synthesis and structurally enhanced photocatalytic performance", *Environ. Sci. Technol.*, 43 [23] (2009) 8968–8973.
18. G. Panthi, M. Park, H.-Y. Kim, S.-Y. Lee, S.-J. Park, "Electrospun ZnO hybrid nanofibers for photodegradation of

wastewater containing organic dyes: A review", *J. Indust. Eng. Chem.*, **21** (2015) 26–35.
19. C. Li, R. Chen, X. Zhang, S. Shu, J. Xiong, Y. Zheng, W. Dong, "Electrospinning of $CeO_2$-ZnO composite nanofibers and their photocatalytic property", *Mater. Lett.*, **65** [9] (2011) 1327–1330.
20. C. Luo, D. Li, W. Wu, Y. Zhang, C. Pan, "Preparation of porous micro-nano-structure NiO/ZnO heterojunction and its photocatalytic property", *RSC Advances*, **4** [6] (2014) 3090–3095.
21. A. Yar, B. Haspulat, T. Üstün, V. Eskizeybek, A. Avcı, H. Kamış, S. Achour, "Electrospun $TiO_2$/ZnO/PAN hybrid nanofiber membranes with efficient photocatalytic activity", *RSC Advances*, **7** [47] (2017) 29806–29814.
22. H. Kawazoe, M. Yasukawa, H. Hyodo, M. Kurita, H. Yanagi, H. Hosono, "P-type electrical conduction in transparent thin films of $CuAlO_2$", *Nature*, **389** [6654] (1997) 939–942.
23. H. Yanagi, H. Kawazoe, A. Kudo, M. Yasukawa, H. Hosono, "Chemical design and thin film preparation of p-type conductive transparent oxides", *J. Electroceram.*, **4** [2-3] (2000) 407–414.
24. D.O. Scanlon, G.W. Watson, "Understanding the p-type defect chemistry of $CuCrO_2$", *J. Mater. Chem.*, **21** [11] (2011) 3655–3663.
25. W. Ketir, A. Bouguelia, M. Trari, "$NO_3^-$ removal with a new delafossite $CuCrO_2$ photocatalyst", *Desalination*, **244** [1-3] (2009) 144–152.
26. W. Ketir, A. Bouguelia, M. Trari, "Visible light induced $NO_2^-$ removal over $CuCrO_2$ catalyst", *Water Air Soil Pollution*, **199** [1-4] (2009) 115–122.
27. T. Ahmad, R. Phul, P. Alam, I.H. Lone, M. Shahazad, J. Ahmed, T. Ahamad, S.M. Alshehri, "Dielectric, optical and enhanced photocatalytic properties of $CuCrO_2$ nanoparticles", *RSC Advances*, **7** [44] (2017) 27549–27557.
28. W. Ketir, G. Rekhila, M. Trari, A. Amrane, "Preparation, characterization and application of $CuCrO_2$/ZnO photocatalysts for the reduction of Cr(VI)", *J. Environm. Sci.*, **24** [12] (2012) 2173–2179.
29. Z.-Y. Liu, G.-Y. Wang, X.-P. Liu, Y.-J. Wang, "Preparation of $CuCrO_2$ and the photocatalytic properties of its composites", *J. Fuel Chem. Technol.*, **41** [12] (2013) 1473–1480.
30. W. Ketir, M. Trari, Y. Bessekhouad, "Visible light induced HCl splitting over the hetero-system p-$CuCrO_2$/n-$WO_3$", *Renewable Energy*, **69** (2014) 1–6.
31. D. Xiong, H. Chang, Q. Zhang, S. Tian, B. Liu, X. Zhao, "Preparation and characterization of $CuCrO_2$/$TiO_2$ heterostructure photocatalyst with enhanced photocatalytic activity", *Appl. Surf. Sci.*, **347** (2015) 747–754.
32. T. Cossuet, J. Resende, L. Rapenne, O. Chaix-Pluchery, C. Jiménez, G. Renou, A.J. Pearson, R.L. Hoye, D. Blanc-Pelissier, N.D. Nguyen, "ZnO/$CuCrO_2$ core-shell nanowire heterostructures for self-powered UV photodetectors with fast response", *Adv. Funct. Mater.*, **28** [43] (2018) 1803142.
33. J. Fang, H. Fan, Y. Ma, Z. Wang, Q. Chang, "Surface defects control for ZnO nanorods synthesized by quenching and their anti-recombination in photocatalysis", *Appl. Surf. Sci.*, **332** (2015) 47–54.
34. V. Buscio, S. Brosillon, J. Mendret, M. Crespi, C. Gutiérrez-Bouzán, "Photocatalytic membrane reactor for the removal of CI Disperse Red 73", *Materials*, **8** [6] (2015) 3633–3647.
35. Z. Zhang, C. Shao, X. Li, C. Wang, M. Zhang, Y. Liu, "Electrospun nanofibers of p-type NiO/n-type ZnO heterojunctions with enhanced photocatalytic activity", *ACS Appl. Mater. Interfaces*, **2** [10] (2010) 2915–2923.
36. D. Lin, H. Wu, R. Zhang, W. Zhang, W. Pan, "Facile synthesis of heterostructured ZnO-ZnS nanocables and enhanced photocatalytic activity", *J. Am. Ceram. Soc.*, **93** [10] (2010) 3384–3389.
37. J.J. Wu, S.C. Liu, "Low-temperature growth of well-aligned ZnO nanorods by chemical vapor deposition", *Adv. Mater.*, **14** [3] (2002) 215–218.
38. B. Liu, H.C. Zeng, "Hydrothermal synthesis of ZnO nanorods in the diameter regime of 50 nm", *J. Am. Chem. Soc.*, **125** [15] (2003) 4430–4431.
39. G. Wu, T. Xie, X. Yuan, Y. Li, L. Yang, Y. Xiao, L. Zhang, "Controlled synthesis of ZnO nanowires or nanotubes via sol-gel template process", *Solid State Commun.*, **134** [7] (2005) 485–489.
40. J.-A. Park, J. Moon, S.-J. Lee, S.-C. Lim, T. Zyung, "Fabrication and characterization of ZnO nanofibers by electrospinning", *Curr. Appl. Phys.*, **9** [3] (2009) S210–S212.
41. D.C. Look, G.C. Farlow, P. Reunchan, S. Limpijumnong, S. Zhang, K. Nordlund, "Evidence for native-defect donors in n-type ZnO", *Phys. Rev. Lett.*, **95** [22] (2005) 225502.
42. P. Singh, K. Mondal, A. Sharma, "Reusable electrospun mesoporous ZnO nanofiber mats for photocatalytic degradation of polycyclic aromatic hydrocarbon dyes in wastewater", *J. Colloid Interface Sci.*, **394** (2013) 208–215.
43. X. Dong, P. Yang, Y. Liu, C. Jia, D. Wang, J. Wang, L. Chen, Q. Che, "Morphology evolution of one-dimensional ZnO nanostructures towards enhanced photocatalysis performance", *Ceram. Int.*, **42** [1] (2016) 518–526.
44. X. Li, Y. Cheng, S. Kang, J. Mu, "Preparation and enhanced visible light-driven catalytic activity of ZnO microrods sensitized by porphyrin heteroaggregate", *Appl. Surf. Sci.*, **256** [22] (2010) 6705–6709.
45. D. Xiong, Z. Xu, X. Zeng, W. Zhang, W. Chen, X. Xu, M. Wang, Y.-B. Cheng, "Hydrothermal synthesis of ultrasmall $CuCrO_2$ nanocrystal alternatives to NiO nanoparticles in efficient p-type dye-sensitized solar cells", *J. Mater. Chem.*, **22** [47] (2012) 24760–24768.
46. I.C. Kaya, M.A. Sevindik, H. Akyıldız, "Characteristics of Fe-and Mg-doped $CuCrO_2$ nanocrystals prepared by hydrothermal synthesis", *J. Mater. Sci. Mater. Electron.*, **27** [3] (2016) 2404–2411.
47. Ö.A. Yıldırım, C. Durucan, "Room temperature synthesis of Cu incorporated ZnO nanoparticles with room temperature ferromagnetic activity: Structural, optical and magnetic characterization", *Ceram. Int.*, **42** [2, Part B] (2016) 3229–3238.
48. R. Shannon, "Revised effective ionic radii and systematic studies of interatomic distances in halides and chalcogenides", *Acta Crystallogr., Sect. A: Found. Crystallogr.*, **32** [5] (1976) 751–767.
49. C. Wagner, L. Gale, R. Raymond, "Two-dimensional chemical state plots: a standardized data set for use in identifying chemical states by X-ray photoelectron spectroscopy", *Anal. Chem.*, **51** [4] (1979) 466–482.
50. M. Futsuhara, K. Yoshioka, O. Takai, "Structural, electrical and optical properties of zinc nitride thin films prepared by reactive rf magnetron sputtering", *Thin Solid Films*, **322**

[1-2] (1998) 274–281.
51. J. Mass, P. Bhattacharya, R.S. Katiyar, "Effect of high substrate temperature on Al-doped ZnO thin films grown by pulsed laser deposition", *Mater. Sci. Eng. B*, **103** [1] (2003) 9–15.
52. T. Arnold, D. Payne, A. Bourlange, J. Hu, R. Egdell, L. Piper, L. Colakerol, A. De Masi, P.-A. Glans, T. Learmonth, "X-ray spectroscopic study of the electronic structure of $CuCrO_2$", *Phys. Rev. B*, **79** [7] (2009) 075102.
53. S. Poulston, P.M. Parlett, P. Stone, M. Bowker, "Surface oxidation and reduction of CuO and $Cu_2O$ studied using XPS and XAES", *Surf. Interface Anal.*, **24** [12] (1996) 811–820.
54. D. Xiong, H. Wang, W. Zhang, X. Zeng, H. Chang, X. Zhao, W. Chen, Y.-B. Cheng, "Preparation of p-type $AgCrO_2$ nanocrystals through low-temperature hydrothermal method and the potential application in p-type dye-sensitized solar cell", *J. Alloys Compd.*, **642** (2015) 104–110.
55. I.C. Kaya, H. Akyildiz, "Production and characterization of magnesium-doped copper chromite fibers", *Phys. Status Solidi A*, **215** (2018) 1700795.
56. S. Zhou, X. Fang, Z. Deng, D. Li, W. Dong, R. Tao, G. Meng, T. Wang, X. Zhu, "Hydrothermal synthesis and characterization of $CuCrO_2$ laminar nanocrystals", *J. Cryst. Growth*, **310** [24] (2008) 5375–5379.
57. J. Ding, H. Yang, W. Deng, "Optical and photoelectrochemical performance study based on n-ZnO nanorod arrays/p-$CuAlO_2$ laminar films/Ni heterojunction", *Superlattice Microstr.*, **70** (2014) 33–38.
58. C. Boukaous, B. Benhaoua, A. Telia, S. Ghanem, "Effect of copper doping sol-gel ZnO thin films: physical properties and sensitivity to ethanol vapor", *Mater. Res. Express*, **4** [10] (2017) 105024.
59. Z.N. Kayani, M. Siddiq, S. Riaz, S. Naseem, "Optical, magnetic and structural properties of Cr-doped ZnO thin films by sol-gel dip-coating method", *Mater. Res. Express*, **4** [9] (2017) 096403.
60. L. Shi, F. Wang, Y. Wang, D. Wang, B. Zhao, L. Zhang, D. Zhao, D. Shen, "Photoluminescence and photocatalytic properties of rhombohedral $CuGaO_2$ nanoplates", *Sci. Reports*, **6** (2016) 21135.
61. R. Zuo, G. Du, W. Zhang, L. Liu, Y. Liu, L. Mei, Z. Li, "Photocatalytic degradation of methylene blue using $TiO_2$ impregnated diatomite", *Adv. Mater. Sci. Eng.*, **2014** (2014) 170148.
62. A. Houas, H. Lachheb, M. Ksibi, E. Elaloui, C. Guillard, J.-M. Herrmann, "Photocatalytic degradation pathway of methylene blue in water", *Appl. Catal. B*, **31** [2] (2001) 145–157.
63. Z. Zhang, C. Shao, X. Li, L. Zhang, H. Xue, C. Wang, Y. Liu, "Electrospun nanofibers of ZnO-$SnO_2$ heterojunction with high photocatalytic activity", *J. Phys. Chem. C*, **114** [17] (2010) 7920–7925.
64. P. Zhang, L. Wang, X. Zhang, J. Hu, G. Shao, "Three-dimensional porous networks of ultra-long electrospun $SnO_2$ nanotubes with high photocatalytic performance", *Nano-Micro Lett.*, **7** [1] (2015) 86–95.
65. J. Wang, Y.-J. Lee, J.W. Hsu, "Sub-10 nm copper chromium oxide nanocrystals as a solution processed p-type hole transport layer for organic photovoltaics", *J. Mater. Chem. C*, **4** [16] (2016) 3607–3613.
66. F. Guo, W. Shi, H. Wang, M. Han, H. Li, H. Huang, Y. Liu, Z. Kang, "Facile fabrication of a CoO/g-$C_3N_4$ p-n heterojunction with enhanced photocatalytic activity and stability for tetracycline degradation under visible light", *Catalysis Sci. Technol.*, **7** [15] (2017) 3325–3331.
67. H. Derikvandi, A. Nezamzadeh-Ejhieh, "Synergistic effect of p-n heterojunction, supporting and zeolite nanoparticles in enhanced photocatalytic activity of NiO and $SnO_2$", *J. Colloid Interface Sci.*, **490** (2017) 314–327.
68. V. Stevanović, S. Lany, D.S. Ginley, W. Tumas, A. Zunger, "Assessing capability of semiconductors to split water using ionization potentials and electron affinities only", *Phys. Chem. Chem. Phys.*, **16** [8] (2014) 3706–3714.
69. F. Dong, Z. Wang, Y. Li, W.-K. Ho, S. Lee, "Immobilization of polymeric g-$C_3N_4$ on structured ceramic foam for efficient visible light photocatalytic air purification with real indoor illumination", *Environ. Sci. Technol.*, **48** [17] (2014) 10345–10353.